Electronic Supplementary Material (ESI) for Nanoscale.

Supplementary information for

Deriving 2D M_2X_3 (M=Mo, W, X=S, Se) by periodic assembly of chalcogen vacancy lines in their MX_2 counterparts

Xiaowei Wang, ‡[a] Xiaoxiao Guan, ‡[b] Xibiao Ren, ‡[a] Tian Liu, [b] Wei Huang, [a] Juexian Cao *[b] and Chuanhong Jin *[a, b]

[a]State Key Laboratory of Silicon Materials, School of Materials Science and Engineering, Zhejiang University, Hangzhou, Zhejiang 310027, China.

[b]Hunan Institute of Advanced Sensing and Information Technology, Xiangtan University, Xiangtan 411105, China.

‡These authors contributed equally to the paper.

*Corresponding authors: jxcao@xtu.edu.cn; chhjin@zju.edu.cn

This PDF file includes:

Supplementary Movie Description:

The movie shows the formation process from vacancy lines to a Mo_2S_3 domain and its further growth in width (y-axis). The electron probe was put to scan across the Mo_2S_3-MoS_2 interface. During this process, sometimes the magnification was switched to a higher one to accelerate the sulfur removal around the interface, thus leading to the growth of as-formed Mo_2S_3 domains. And we also adjusted the sample position to put the Mo_2S_3-MoS_2

interface in the center of the scanning area. The sample movement and magnification change will blur STEM images. Thus, in this supplementary movie, we deleted those blurring slices to make it more reader-friendly.

1. Structures of vacancy line and structural differences compared to ML-Mo_2S_3

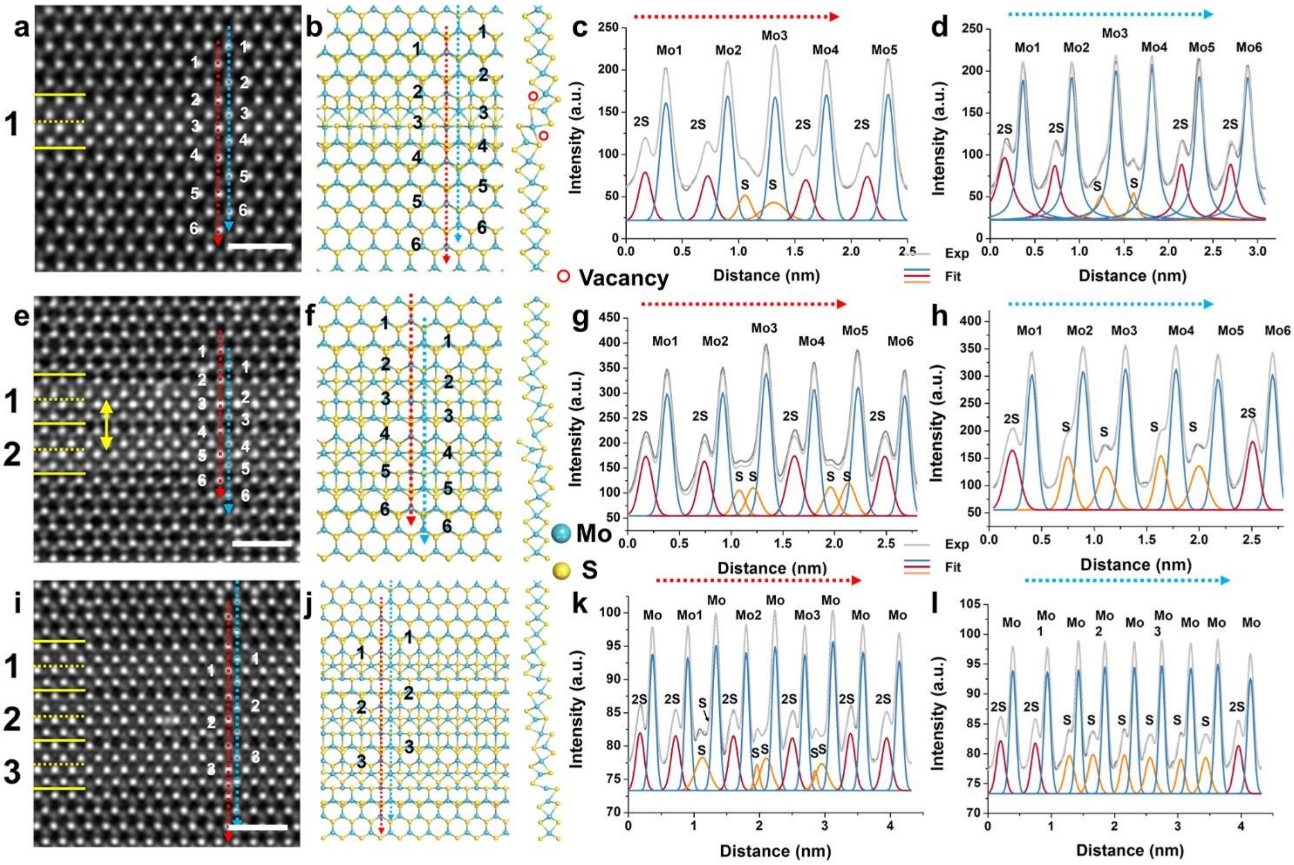

Fig. S1. Vacancy lines in MoS_2. (a, e, i) Atomic resolution ADF-STEM images of 1, 2, and 3 vacancy lines in MoS_2, respectively. (b, f, j) The corresponding structural models of (a, e, i). The red circles in b indicate the di-vacancy feature of vacancy line. (c, d, g, h, k, l) Intensity line profiles in (a, e, i). Scale bar: 1 nm.

We will first discuss the structural difference between the ML-Mo_2S_3 and initial assembled vacancy lines. As indicated by Fig. S2a, b, the difference of a certain bond length between Mo_2S_3 and assembled vacancy lines was defined as: $\sigma_{i,j} = (d_{i,p} - d_{i,j,})^2$, where i represents a certain bond length (e.g. d_{A1} as illustrated in Fig. S2a, b), j represents a certain unit (e.g. U_2 as illustrated in Fig. S2c), p, l represent Mo_2S_3 and vacancy lines, respectively. The total difference of unit j (as illustrated in Fig. S2c) was defined as: $\sigma_j = \sum_i \sigma_{i,j}$. The differences shown in the main text were the average of σ_j in the middle part of assembled defects (red dots in Fig. S2d).

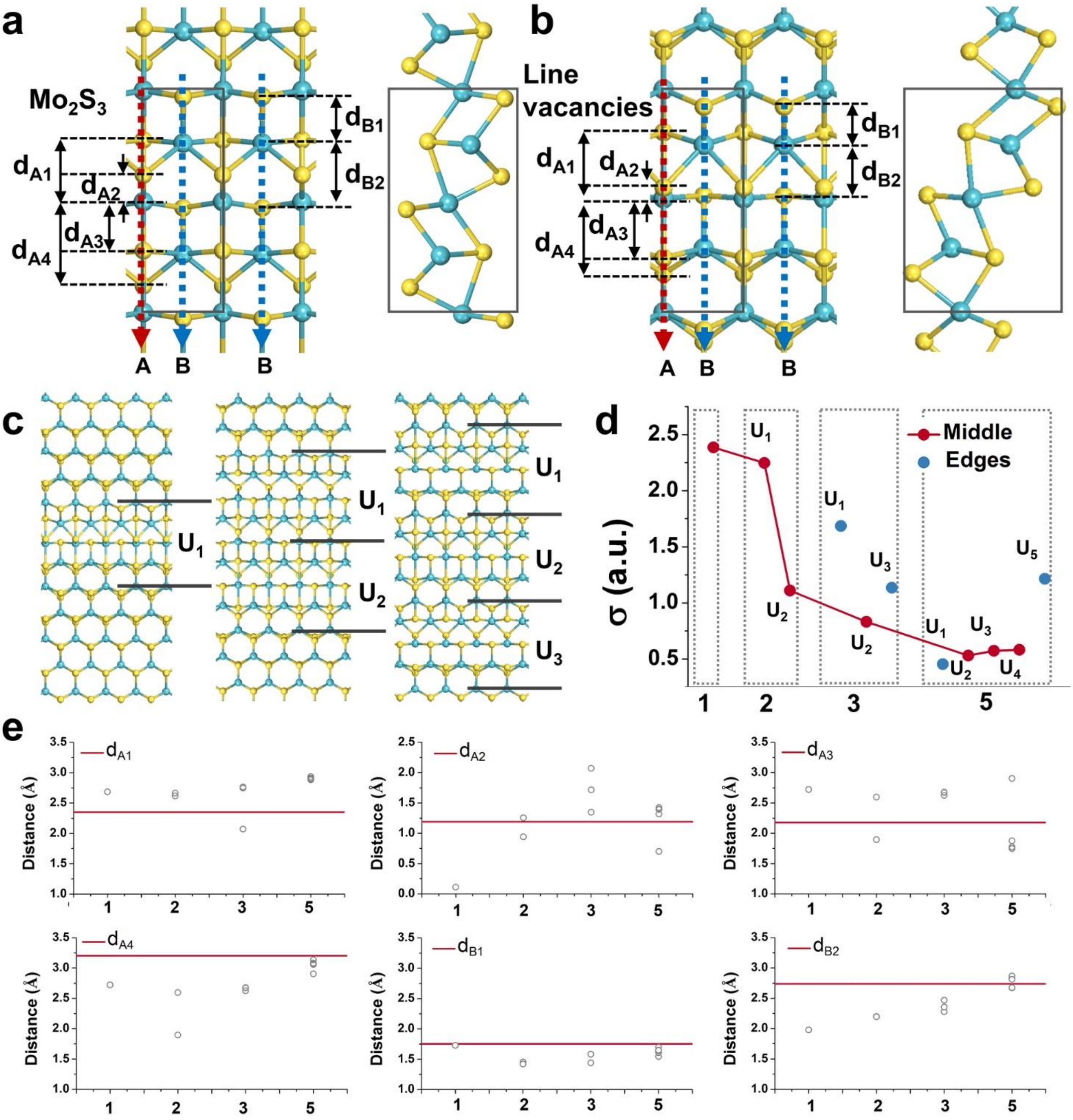

Fig. S2. The structural differences between the Mo$_2$S$_3$ and assembled vacancy lines (σ). (a, b) Typical bond lengths measured in Mo$_2$S$_3$ and corresponding positions in 1 vacancy line in (b. c) Schematic diagram of units in 1, 2, 3 vacancy lines. (d) The differences (σ) between the Mo$_2$S$_3$ and assembled vacancy lines to the number of lines. U$_1$, U$_2$… represent unit 1, unit 2… as illustrated in (c). The red dots represent vacancy lines at the middle part of assembled vacancy lines (such as U$_2$ in 3 vacancy line in (c)), while blue dots represent those at edges (such as U$_1$ and U$_3$ in 3 vacancy lines in (c)). (e)

The differences of bond length between the Mo_2S_3 phase and assembled vacancy lines in certain positions to the number of lines. "d_{A1}", "d_{A2}"… represent typical bond lengths as illustrated in (a, b).

2. Growth of Mo_2S_3 domain in width and length

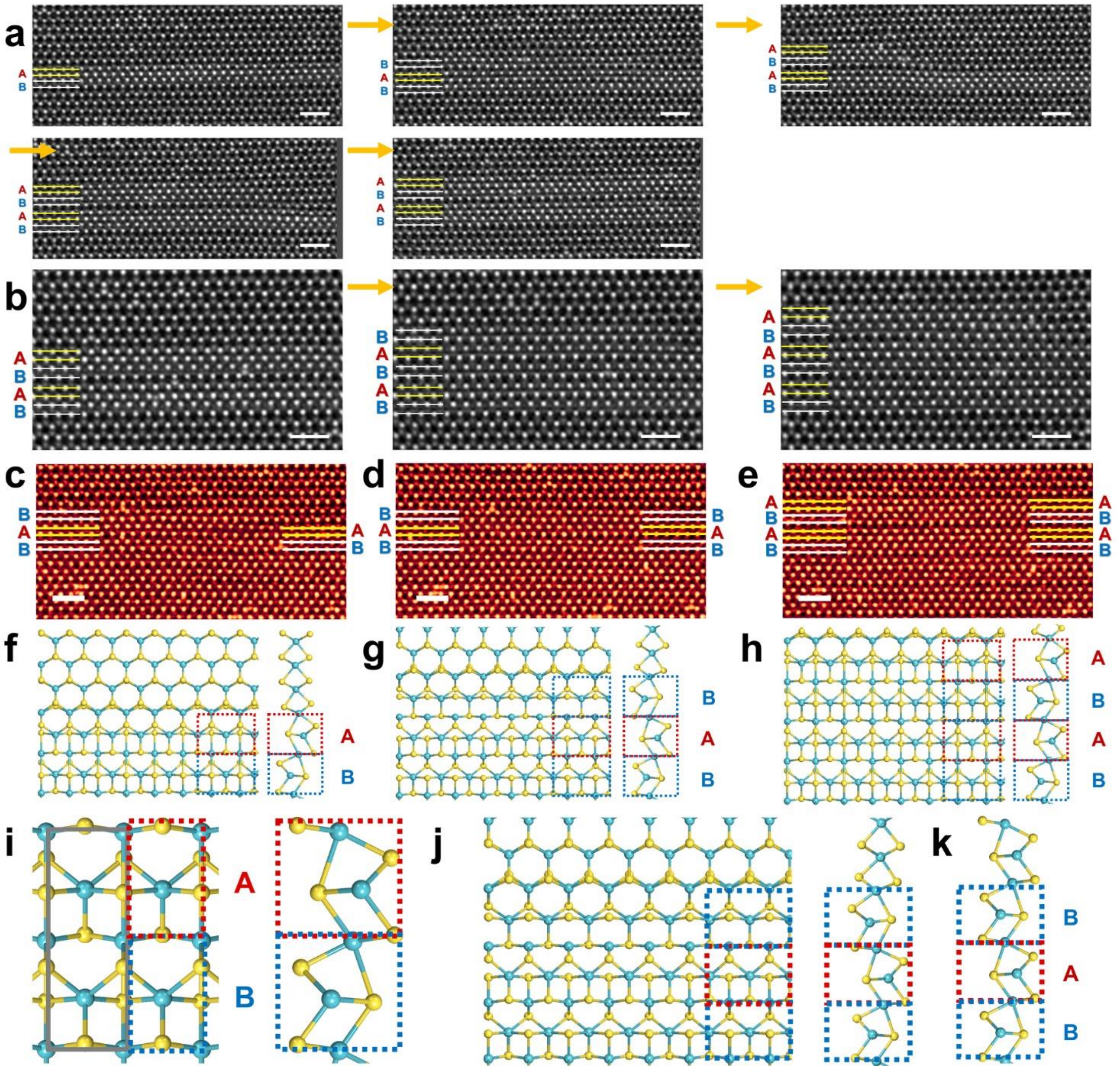

Fig. S3. Growth of Mo_2S_3 in armchair direction. (a, b) Temporal ADF-STEM images of the extension of vacancy lines in y-direction. (a) Extension from 1 vacancy line to 2 vacancy lines; (b) Extension from 2 vacancy lines to 3 vacancy lines. “A” and “B” indicate half unit cell, same as that in i. Scale bars: a: 1 nm; (c-e) Temporal ADF-STEM images of the growth of Mo_2S_3 in y-direction, with their corresponding structural models displayed in (f, g, h). Scale bars: 1 nm. (i) Top and side views of ML-

Mo_2S_3. The red and blue boxes indicate half unit cell. “A” and “B” indicate half unit cell. (j) Top and side views of the interface of Mo_2S_3/MoS_2. (k) Side view of the structural model of Mo_2S_3.

The extensions of Mo_2S_3 domain along armchair direction are accomplished by the step of the half-width of a vacancy line (A or B as shown in Fig. S3i), as indicated in Fig. S3c-e and 3f, h, i. The extension step of half unit cell is due to: 1) The unit cell in Mo_2S_3 can be divided in half, as indicated in Fig. S3i (labeled as A and B). In the top view, the top half unit in Mo_2S_3 in Fig. S3i (B, blue box) is identical to the bottom half unit (A, red box). 2) The structure of the interface between MoS_2/Mo_2S_3 (BAB, BAB represents the sequence of half units in Mo_2S_3) is very similar to that in Mo_2S_3 (BAB), as comparing the side views in Fig. S3j and 3k. Thus, the interface in Fig. S3f (MoS_2/AB) should be identical to that in Fig. S3g (MoS_2/BA) when viewing in z-direction. All in all, the smallest unit in the extension of Mo_2S_3 in y-direction is the half-width of a vacancy line (A or B).

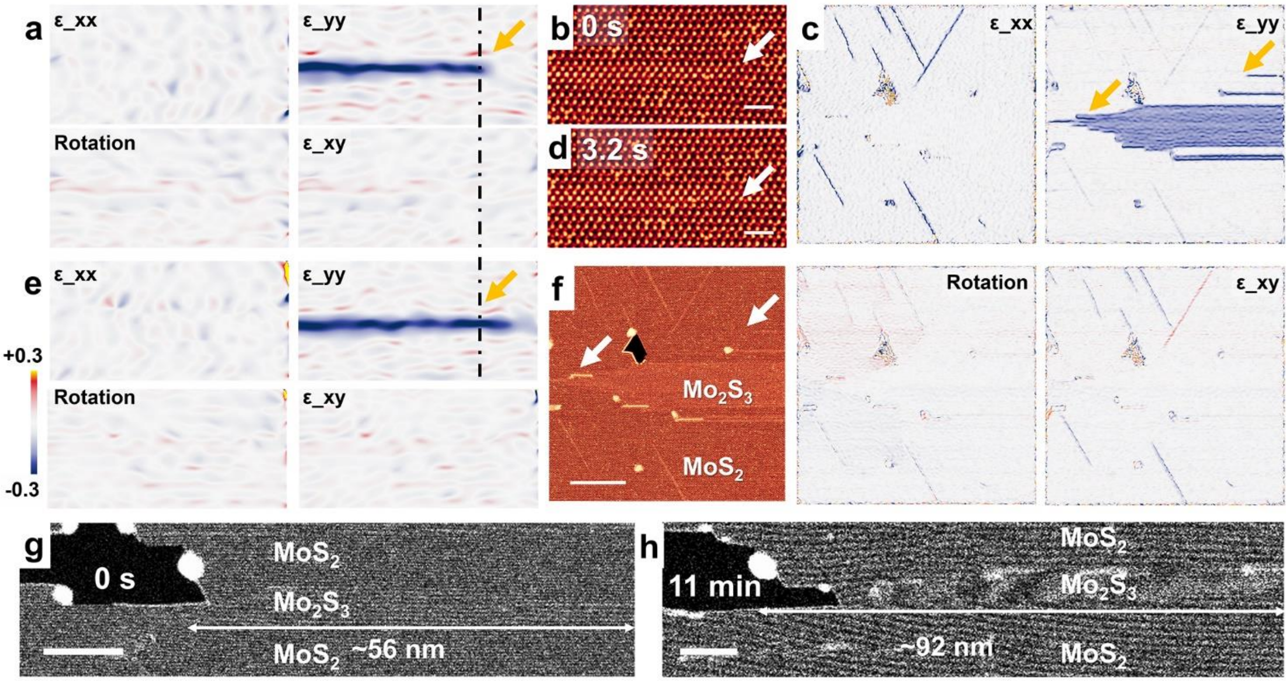

Fig. S4. The strain maps of vacancy lines and Mo_2S_3 in MoS_2 matrix. (a, e) GPA calculated ε_xx, ε_yy, Rotation, ε_xy strain maps in (b, d). The black dot line indicates the growth of line vacancies. (b, d) Temporal ADF-STEM images of vacancy lines. (c), GPA calculated ε_xx, ε_yy, Rotation, ε_xy strain maps in (f). There is no strain (contrast) in ε_xx maps, which further prove the perfect epitaxy of Mo_2S_3 and MoS_2 along zigzag direction. Scale bar: 10 nm. (g-i), Temporal ADF-STEM images of the extension of vacancy lines in x-direction. Scale bars: 10 nm.

3. Appling our method in other TMDCs (WS_2 and WSe_2) and in other types of defects (point defects)

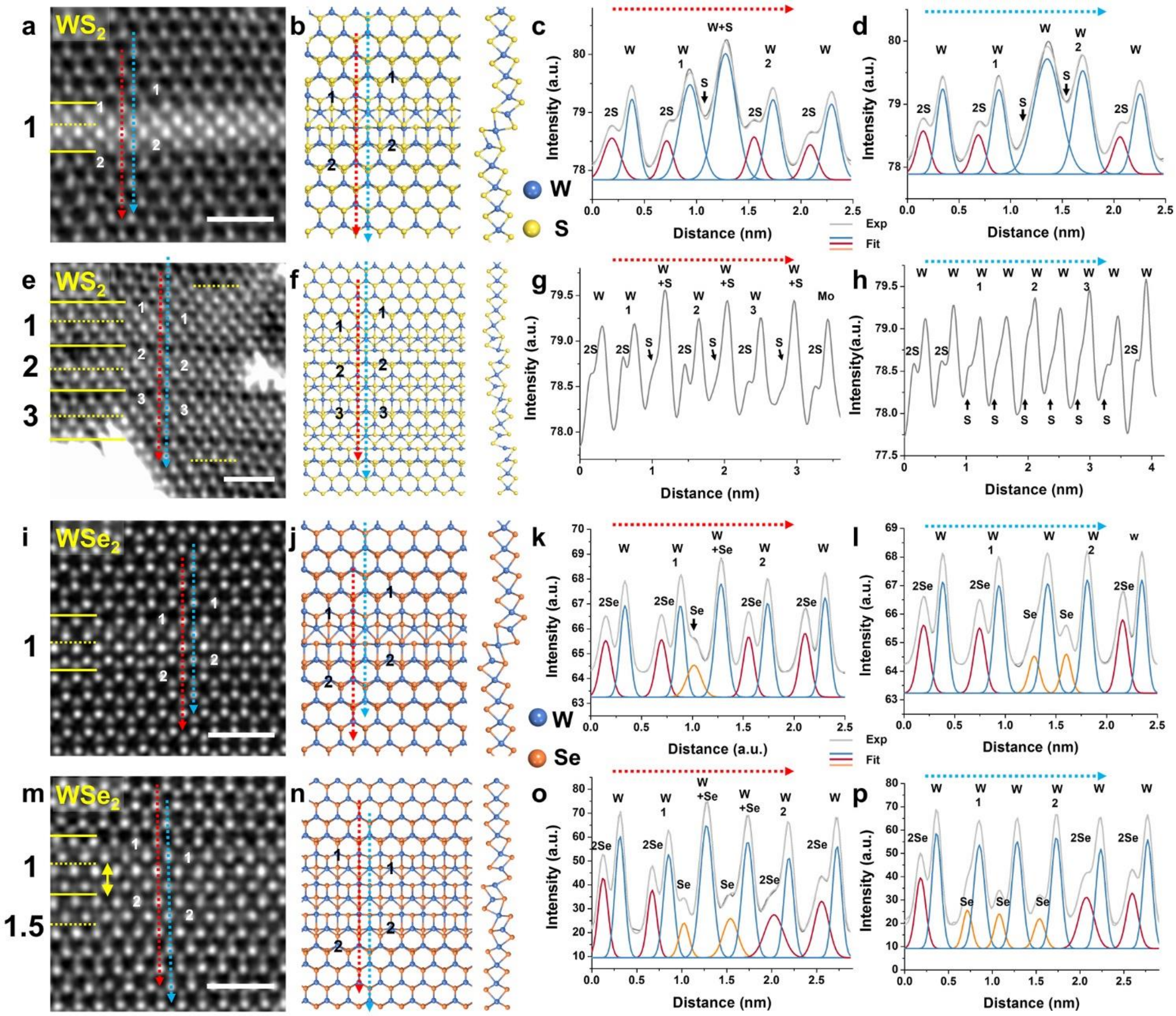

Fig. S5. Chalcogen vacancy lines and M_2X_3 structure in WS_2, and WSe_2, taking similar configuration to that in MoS_2. (a, e, i, m) ADF-STEM images of 1, 3 vacancy lines in WS_2, and 1, 1.5 vacancy lines in WSe_2, respectively. The structures of vacancy lines in WS_2 and WSe_2 are very similar to that in MoS_2, as compared with Fig. S1. (b, f, j, n) Corresponding structural models of (a, e, i, m), respectively. (c, d, g, h, k, l, o, p) Intensity line profiles in (a, e, i, m). Scale bar: 1 nm.

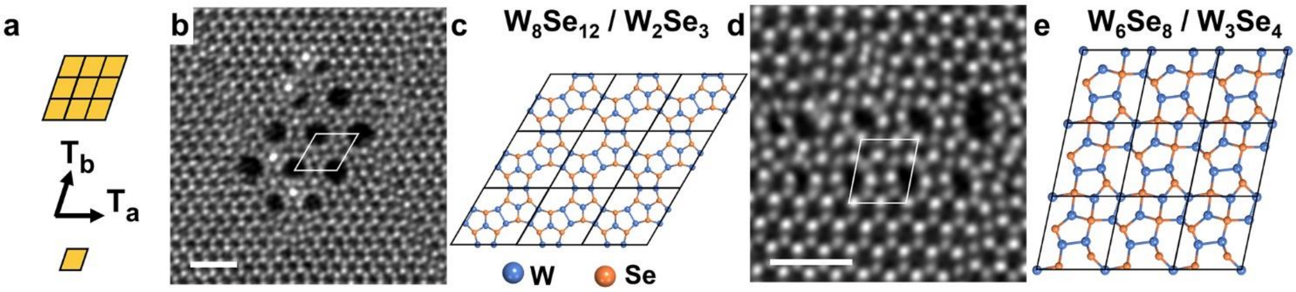

Fig. S6. Assembly of point defects in 2D TMDC materials. (a) Schematic diagram of the transition of ordered point defects into crystal by the periodic assembly. (b, d) Two examples of transition showing the ordered arrangement of point defects (0D) into new structural 2D materials, i.e., W_6Se_8/W_3Se_4 and W_8Se_{12}/W_2Se_3, respectively. And their corresponding structural models are displayed in (c) and (e), respectively. Scale bar: 1 nm.

4. Details about the structure of ML-Mo_2S_3

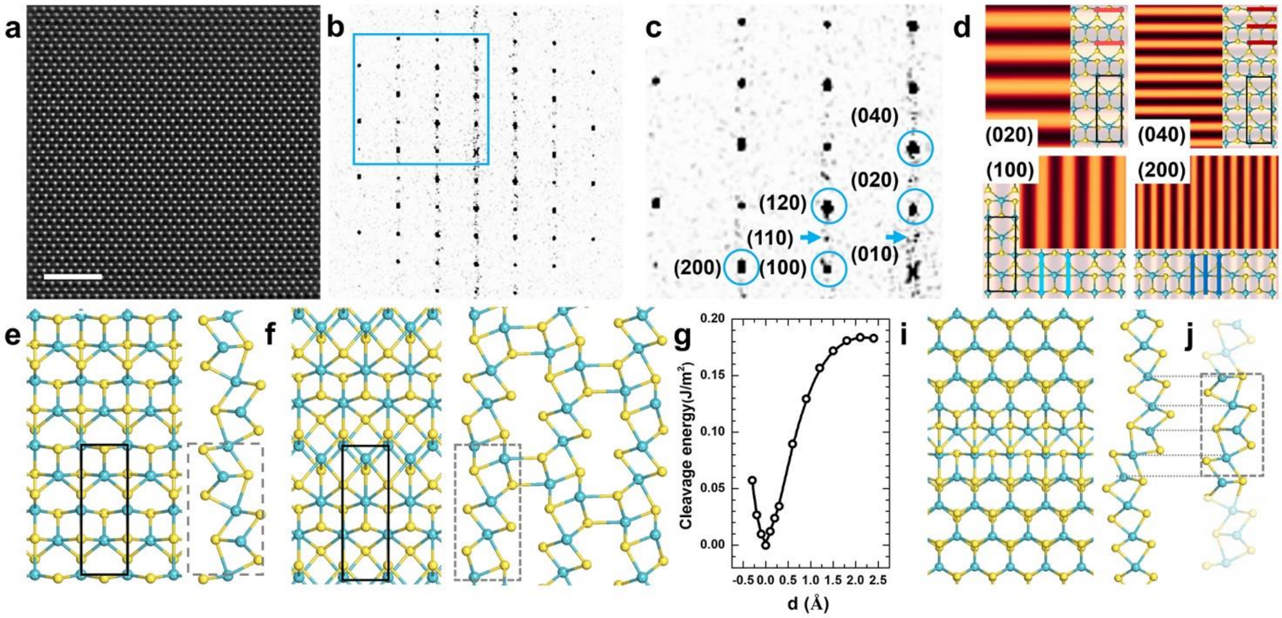

Fig. S7. ML-Mo_2S_3 and bulk Mo_2S_3. (a, b) ADF-STEM images of ML-Mo_2S_3 and its corresponding FFT. (c) Enlarged image of FFT in the blue box in (b). (d) Lattice fringes obtained by inverse FFT of corresponding lattice planes in (c), with the structural models displayed besides. (e, f, i) Top and side views of structural model of ML-Mo_2S_3, Mo_2S_3 bulk and 1 vacancy line, respectively. The black and grey boxes indicate the unit cells. (g) Cleavage energy of Mo_2S_3 bulk to interlayer distance. (j) Side view of ML-Mo_2S_3.

The structure of bulk Mo_2S_3 is shown in Fig. S7f. The side view of bulk Mo_2S_3 indicates that it is also a layer-structure material, and can be easily isolated, with dissociation energy of 0.183 J/m^2 (30 meV/atom) as demonstrated in Fig. S7g. However, the structure of ML-Mo_2S_3 (obtained in our experiments) is dramatically different from the MLB-Mo_2S_3 (exfoliated from bulk Mo_2S_3), as compared with Fig. S7e and 7f. Furthermore, the structure of ML-Mo_2S_3 is very similar to that of the vacancy line, as compared with Fig. S7i and 7j.

5. Structural stability of 2D M_2X_3

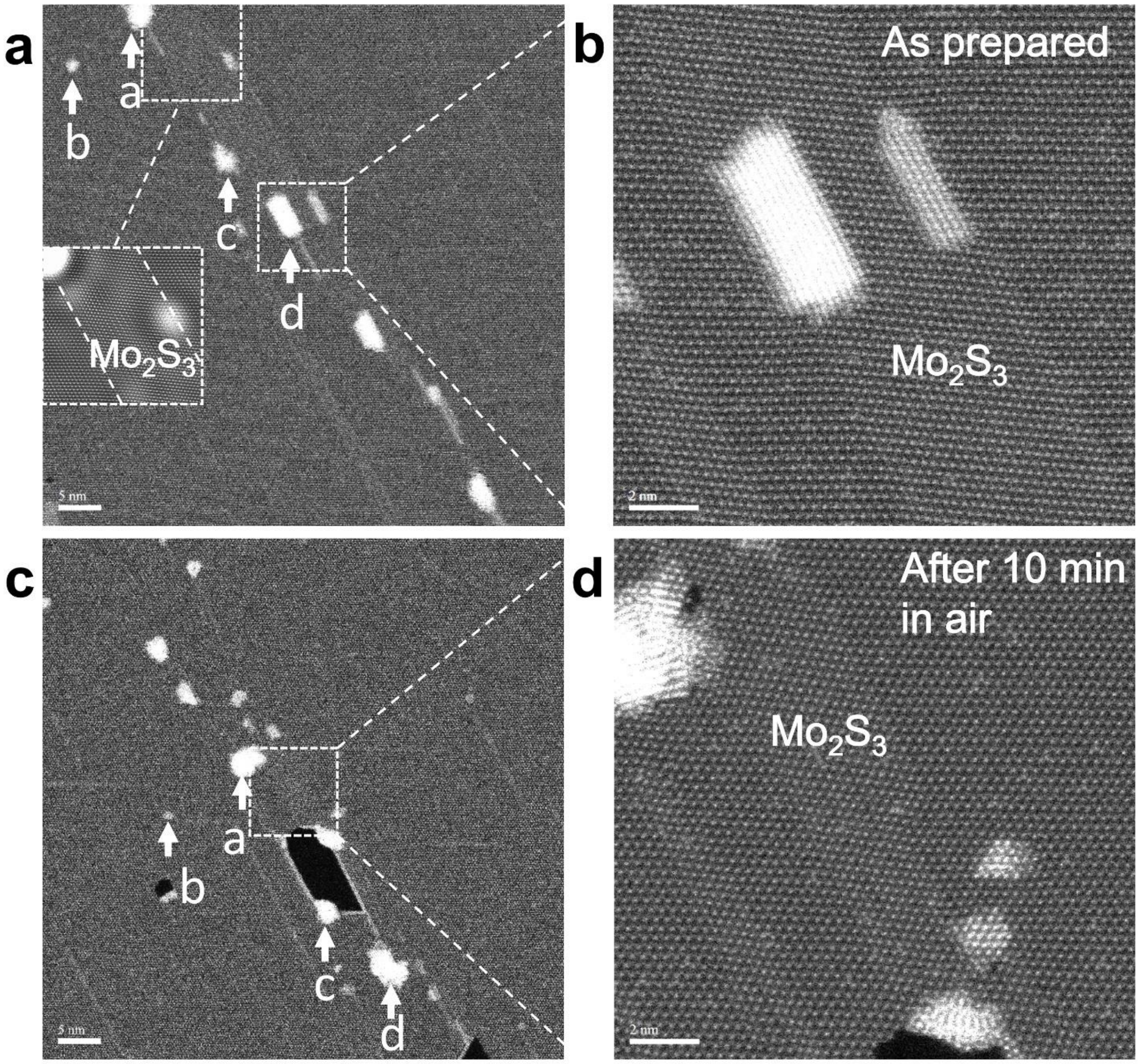

Fig. S8. Air stability of ML-Mo_2S_3. (a, b) ADF-STEM images of Mo_2S_3 before exposing into the air. Inserted on the left: Enlarged filtered image. (c, d) STEM images of Mo_2S_3 after exposing in the air for 10 min. “a”, “b”, “c”, “d”, indicate the adopted Mo cluster which serves as position markers.

To examine the air stability of ML-Mo_2S_3, we exposed the as-formed Mo_2S_3 in the air for 10 mins by pulling out the sample from TEM. We then inserted the sample back into TEM, and observed the changes. STEM images in Fig. S8a, b and 8c, d were acquired at the same position. As indicated by Fig. S8d that, the Mo_2S_3 domain still kept the crystalline state after air exposition. It should be noted that, the hole between positions “a”, “c” were damaged by chemical etching of electron beam during imaging process when we inserted back the sample (To prevent the influence of high temperature on the phase, we conducted the experiments at room temperature, but inevitably lead to the significant chemical etching at room temperature).

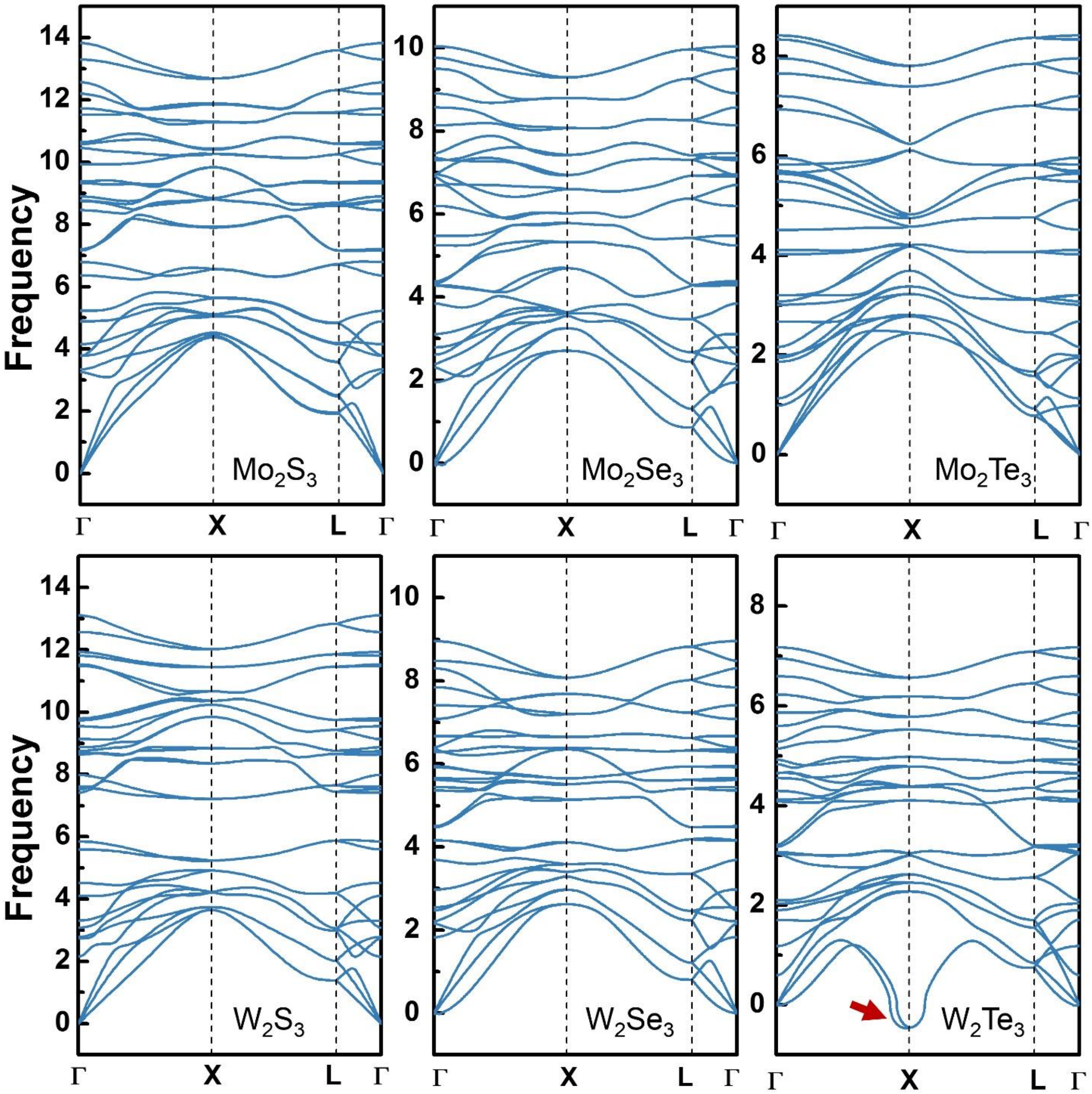

Fig. S9. Phonon dispersion of monolayer Mo_2S_3, Mo_2Se_3, Mo_2Te_3, W_2S_3, W_2Se_3, W_2Te_3, respectively. The phonon spectra were calculated using PHONONPY code. There are no negative phonon frequencies in ML-M_2X_3 (M=Mo,W; X=S, Se, Te) except W_2Te_3, which indicated that these structures are stable.

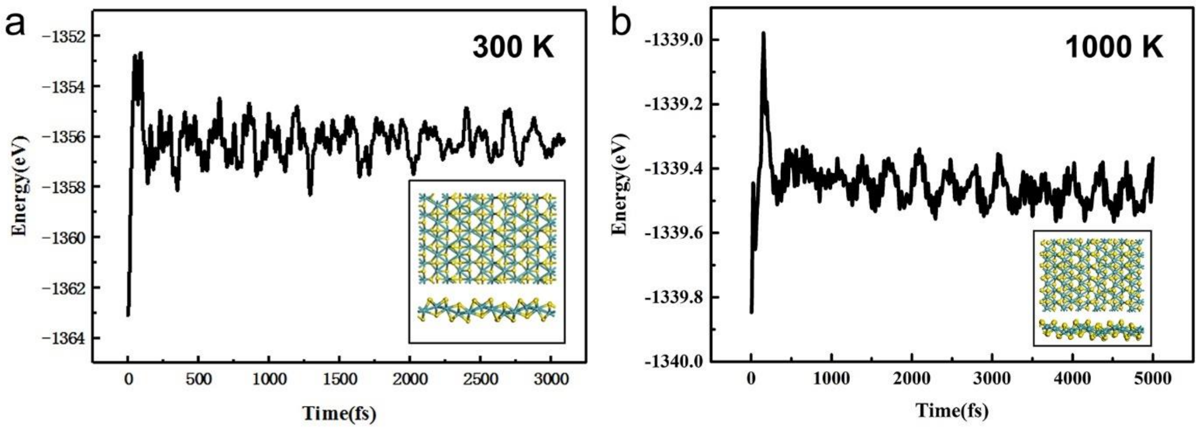

Fig. S10. *Ab initio* molecular dynamics (AIMD) of Mo_2S_3 with the canonical (NVT) ensembles at 300 K (a) and 1000 K (b), respectively.

6. The structural of MoS_{2-x}

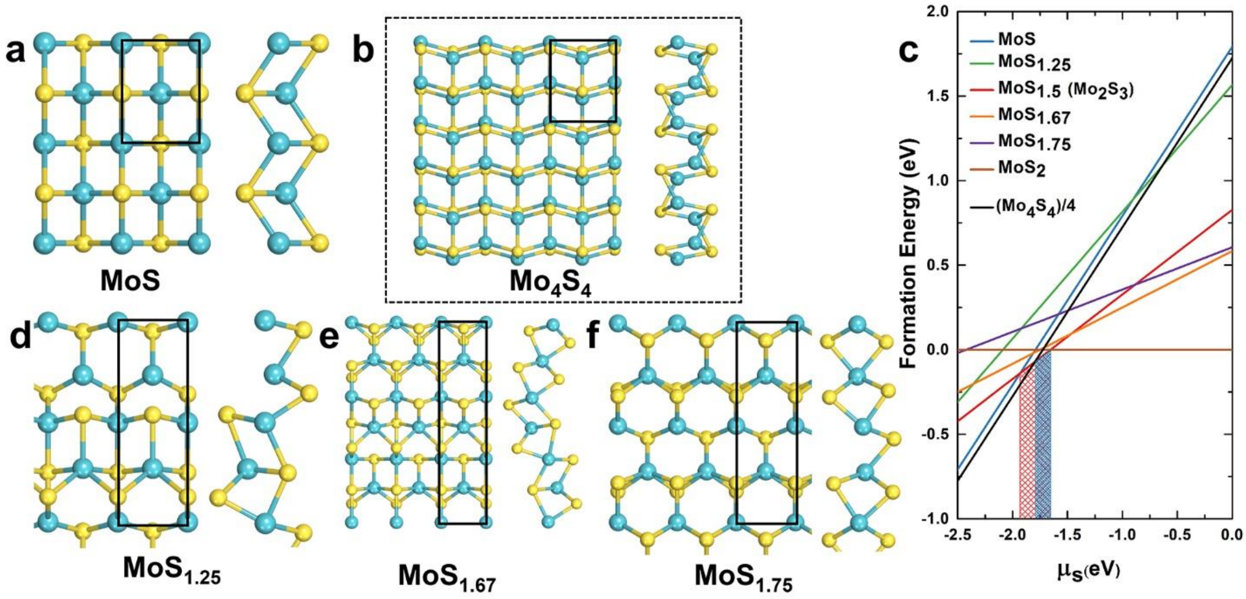

Fig. S11. (a, d-f) DFT-calculated structures of MoS_{2-x} (2-x=1, 1.25, 1.67, 1.75). (b) DFT-calculated structures by previous work[1]. (c) Formation energies of different MoS_{2-x} phase (2-x=1, 1.25, 1.67, 1.75) and Mo_4S_4 (black line, calculated based on the atomic model in a previous study[1]). As seen, ML-Mo_2S_3 becomes the most stable configuration for a chemical potential window $\mu_S \in (-1.79\ \text{eV}, -1.65\ \text{eV})$ over all the structures.

7. Electronic structures and band gaps of ML-M_2X_3

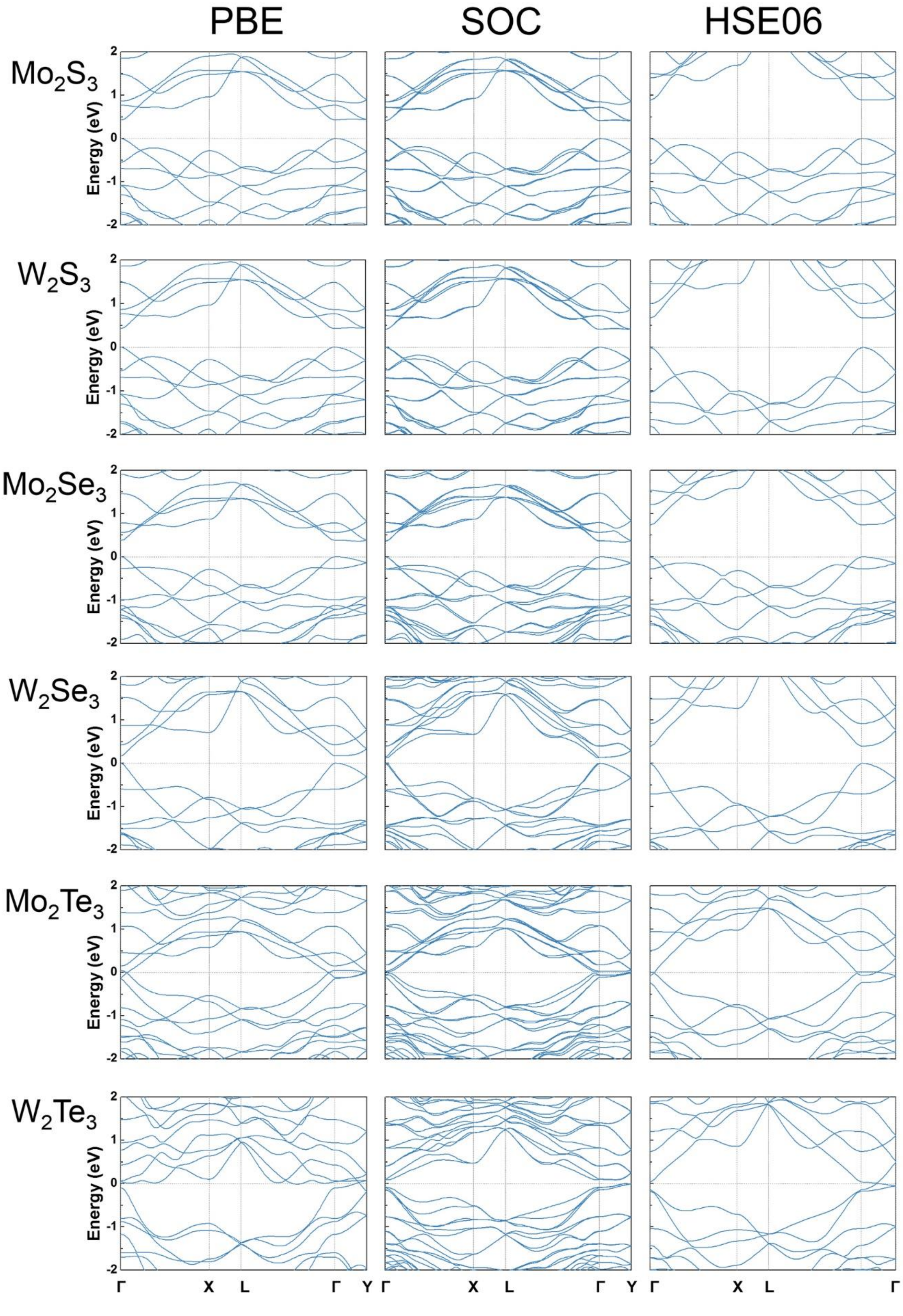

Fig. S12. Electronic band structures of monolayer Mo_2S_3, W_2S_3, Mo_2Se_3, W_2Se_3, Mo_2Te3, W_2Te_3, respectively. They were calculated by PBE without (left) and with (middle) SOC, and also by HSE06 (right).

Table S1. Structural information and band gaps of ML-M_2X_3

Structure	**a**	**b**	**E_g (PBE)**	**E_g (SOC)**	**E_g (HSE06)**
	(Å)			**(eV)**	
MoS_2	3.182	11.025	/	/	/
Mo_2S_3	3.254	9.097	0.429(D)*	0.406(I) †	0.885(D)
W_2S_3	3.239	9.056	0.320(D)	0.325(I)	0.666(D)
Mo_2Se_3	3.351	9.293	0.375(I)	0.339(I)	0.741(D)
W_2Se_3	3.332	9.241	0.173(I)	0.127(I)	0.394(D)
Mo_2Te_3	3.481	9.680	/	/	/
W_2Te_3	3.489	9.613	/	0.085(I)	/

D: Direct**;** I: Indirect

8. Parameters used for calculating carrier mobilities

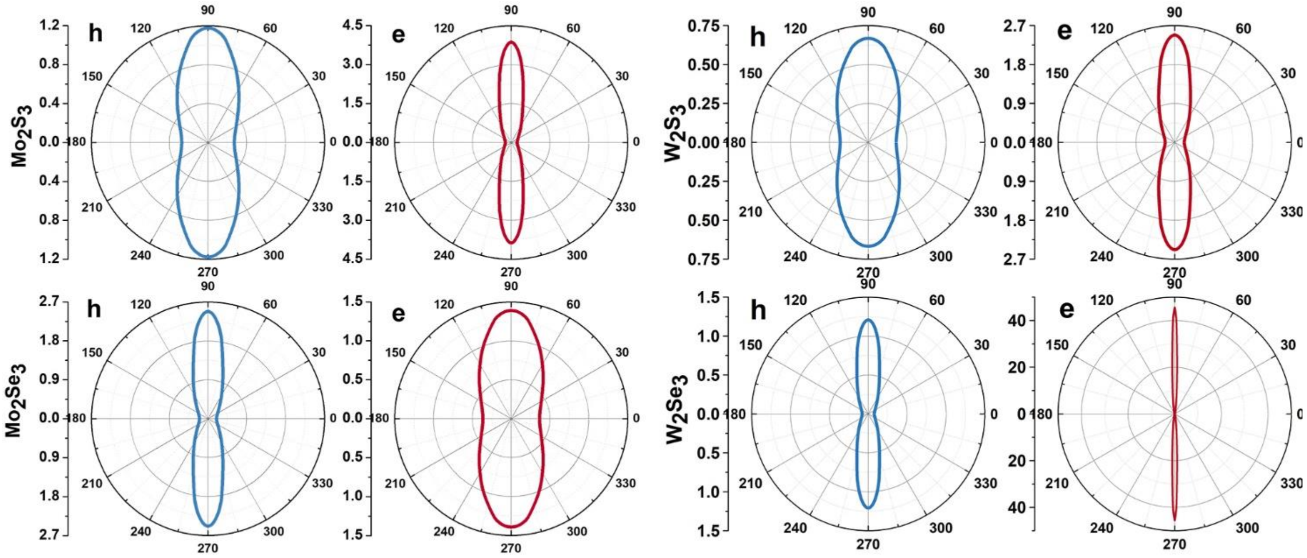

Fig. S13. Carrier effective masses as a function of angle. The direction of x/y-axis is indicated in the atomic model within Fig. 3 in the main text. “h” represents hole while “e” represents electron, respectively. 0° represents x direction while 90° represents y direction. Refer to Fig. 3d in the main text for more details about k space.

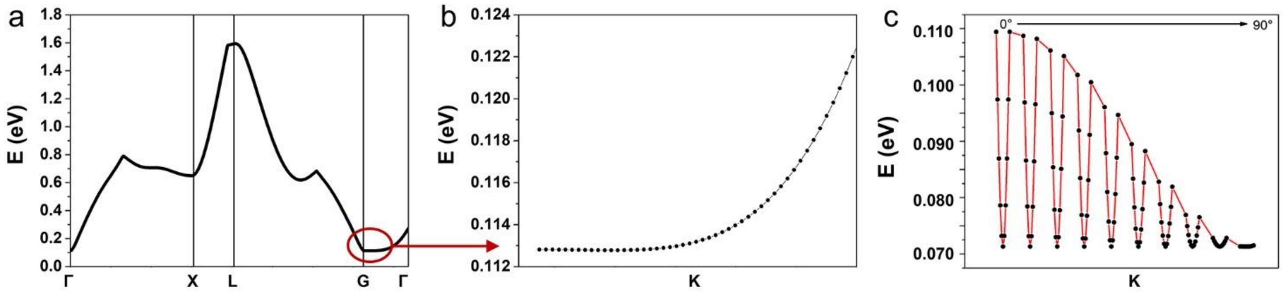

Fig. S14. Detailed analysis for the origin of large effective mass of ML-W$_2$Se$_3$. (a, b) The conduction band structure of ML-W$_2$Se$_3$. (c) The CBM of ML-W$_2$Se$_3$ along different direction. 0° represents x direction while 90° represents y direction. Thus, the flat band feature near CBM along y direction results in the large effective mass of electron (45.518) as shown in Table 1 in the main text.

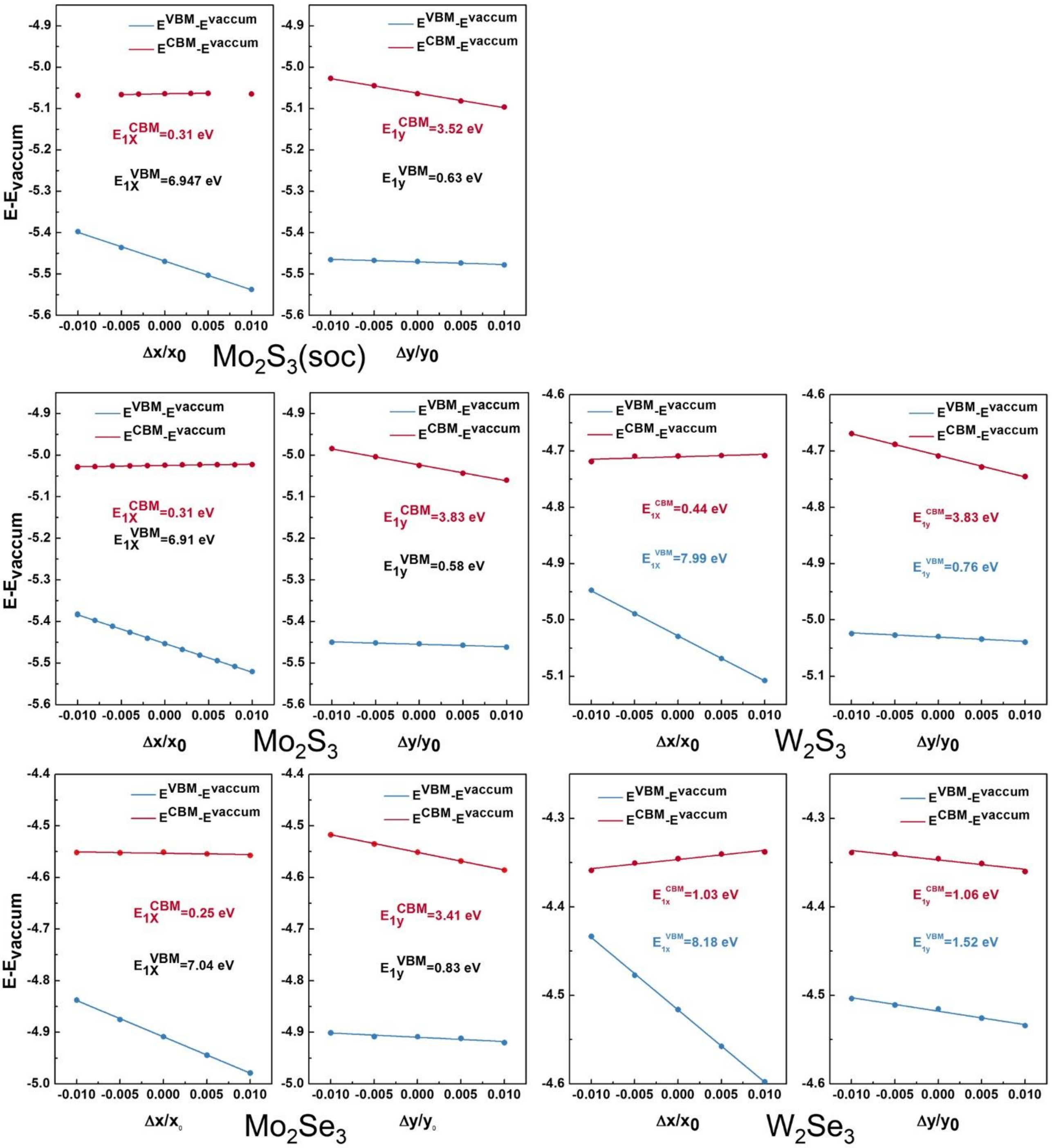

Fig. S15. Band energies of the CBMs and VBMs of monolayer Mo_2S_3, Mo_2Se_3, W_2S_3, W_2Se_3 to the vacuum energy as a function of the lattice dilation, respectively.

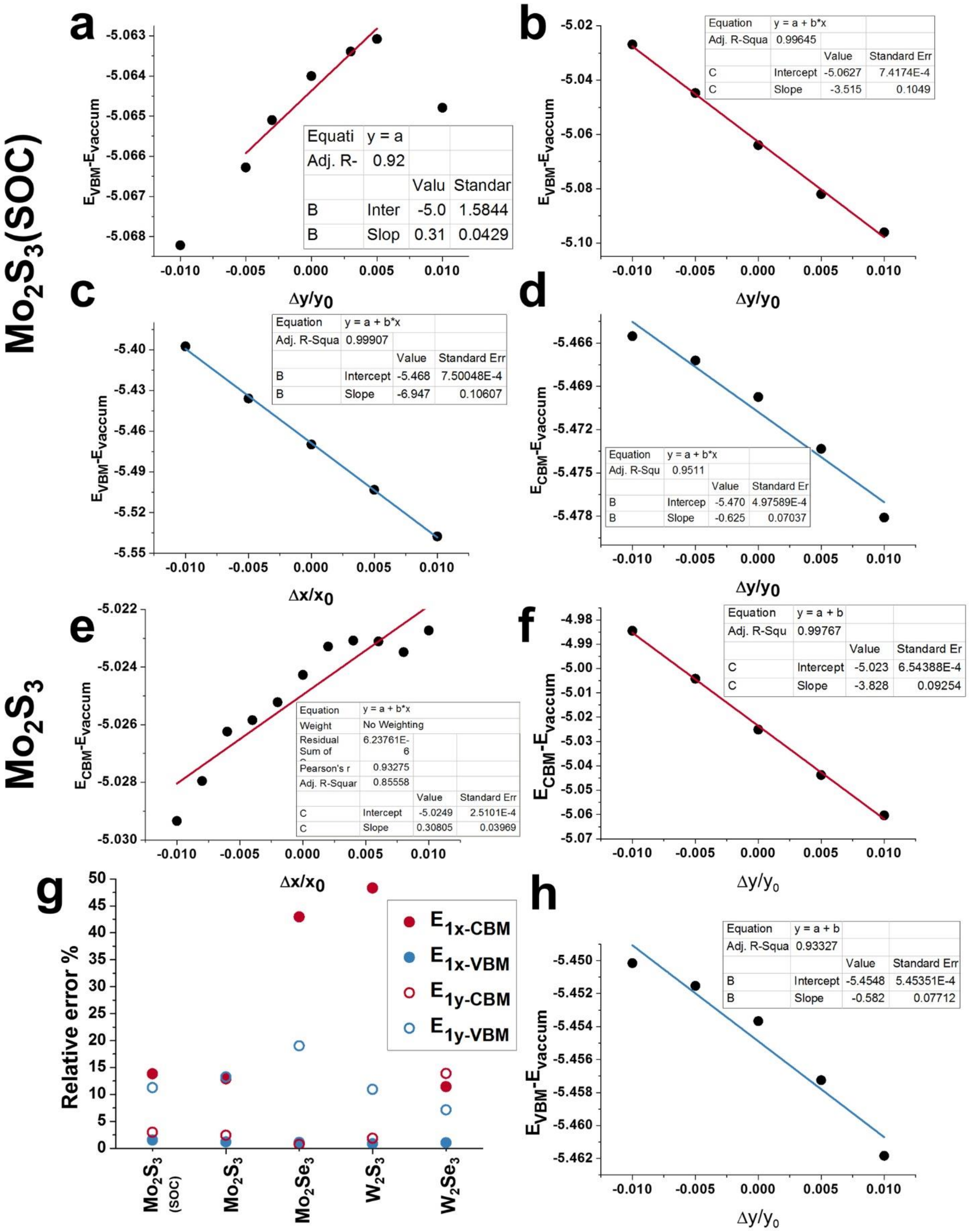

Equati	y = a		
Adj. R-	0.92		
		Valu	Standar
B	Inter	-5.0	1.5844
B	Slop	0.31	0.0429

Equation	y = a + b*x		
Adj. R-Squa	0.99645		
		Value	Standard Err
C	Intercept	-5.0627	7.4174E-4
C	Slope	-3.515	0.1049

Equation	y = a + b*x		
Adj. R-Squa	0.99907		
		Value	Standard Err
B	Intercept	-5.468	7.50048E-4
B	Slope	-6.947	0.10607

Equation	y = a + b*x		
Adj. R-Squ	0.9511		
		Value	Standard Er
B	Intercep	-5.470	4.97589E-4
B	Slope	-0.625	0.07037

Equation	y = a + b*x		
Weight	No Weighting		
Residual Sum of	6.23761E-6		
Pearson's r	0.93275		
Adj. R-Squar	0.85558		
		Value	Standard Err
C	Intercept	-5.0249	2.5101E-4
C	Slope	0.30805	0.03969

Equation	y = a + b		
Adj. R-Squ	0.99767		
		Value	Standard Er
C	Intercept	-5.023	6.54388E-4
C	Slope	-3.828	0.09254

Equation	y = a + b		
Adj. R-Squa	0.93327		
		Value	Standard Err
B	Intercept	-5.4548	5.45351E-4
B	Slope	-0.582	0.07712

Fig. S16. Relative errors on the calculated deformation potential. (a-d) Band energy of the CBM (a, b), VBM (c,d) of ML-Mo_2S_3 to the vacuum energy as a function of lattice dilation, respectively. Here, the band energies were calculated with the PBE potential (SOC considered), and the solid lines are the fitting curves. Insets show the standard errors of the fitted slope, which corresponds to the deformation potential. It should be noted that the linearity of $E_{1x\text{-}CBM}$ is not good in the range of -0.01 to 0.01. Thus, we chose a range from -0.005 to 0.005 for the deformation potential calculation. (e, f, h) Band energy of the CBM (e, f), VBM (h) of ML-Mo_2S_3 to the vacuum energy as a function of lattice dilation, respectively. (g) Summarized Relative errors for the deformation potential of ML-M_2X_3 for the *x* and *y* directions.

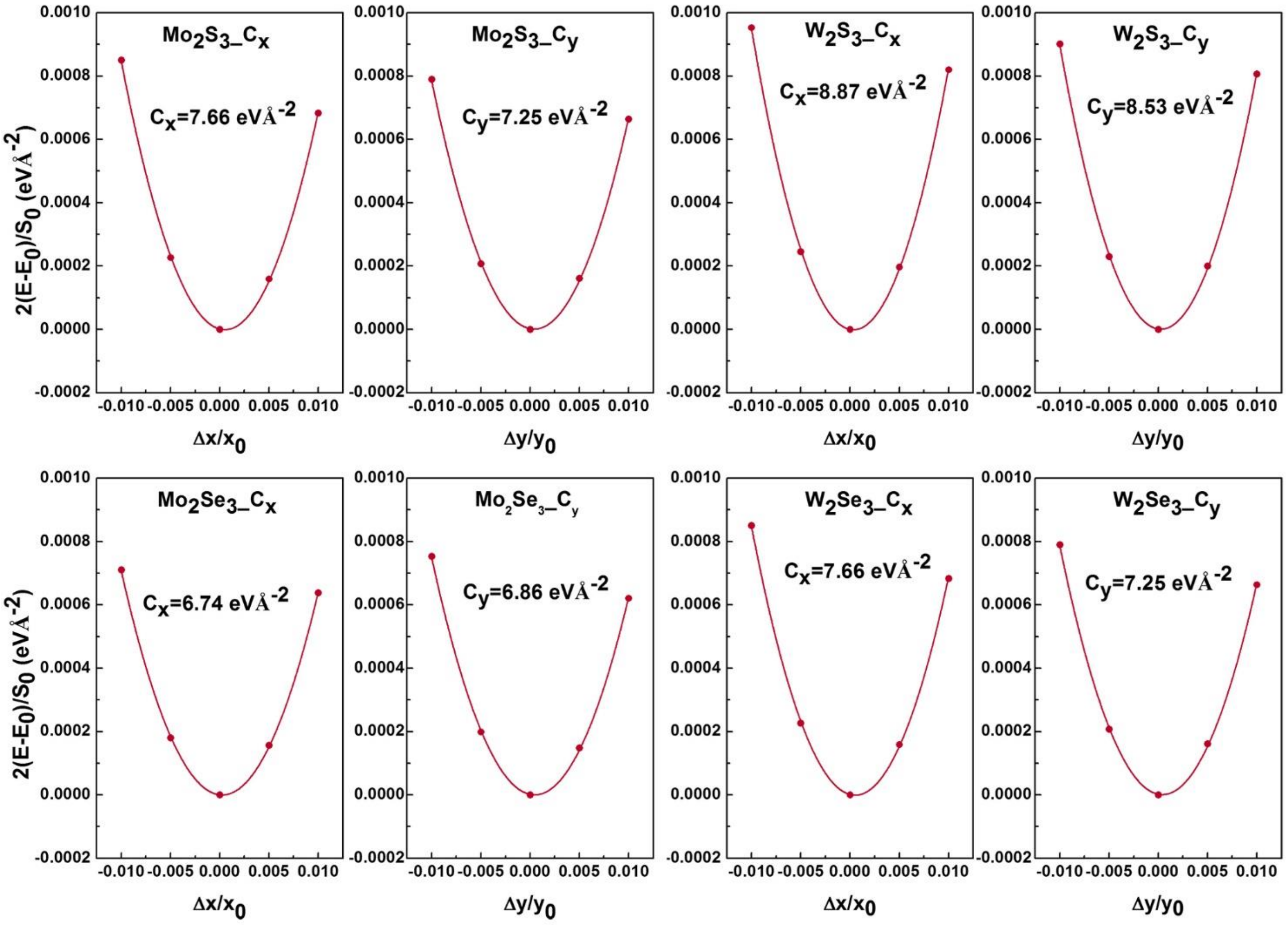

Fig. S17. Calculated elastic moduli in x and y direction of ML-Mo_2S_3, Mo_2Se_3, W_2S_3, W_2Se_3, respectively.

9. Methods for calculating carrier mobilities

$$\mu_{\mathrm{x}} = \frac{e\hbar^3 C_{\mathrm{x}}}{k_B T m_x m_d (E_{1x})^2} \qquad (1)$$

Besides the formalism displayed in the main text (equation (2)) or equation (1) shown above, there are other methods for calculating carrier mobilities. Equation (2) is the formalism for calculating the carrier mobility of anisotropic two-dimensional semiconductors under longitudinal acoustic phonon scattering[3,4].

$$\mu_{2D} = \frac{e\hbar^3 (5C_{\mathrm{x}}+3C_{\mathrm{y}})/8}{k_B T m_x m_d \left(9{E_{1x}}^2+7E_{1x}E_{1y}+4{E_{1y}}^2\right)/20} \qquad (2)$$

where m_x is the effective mass along x direction, m_d is the average effective mass determined by $m_d = \sqrt{m_x m_y}$. C_x (or C_y) and E_{1x} (or E_{1y}) represent elastic modulus and deformation potentials in the propagation direction of the longitudinal acoustic wave, respectively. Similarly, the carrier mobility along the y direction is given by equation (1) and (2) when x is interchanged with y.

And the anisotropic ratio R_{ani} is defined as:

$$R_{ani} = \max(\mu_x, \mu_y) \,/\, \min(\mu_x, \mu_y) \qquad (3)$$

The calculated results are shown in Table S2. In equation (1), the carrier mobility is the function of elastic constant and deformation potential along only the longitudinal charge transport direction. While in equation (2), carrier mobility depends on all the three parameters, namely, elastic constant, carrier effective mass and deformation potential, not only along the longitudinal charge transport direction but also the in-plane transverse direction. It is worth to mention that the method based on equation (1) will overestimate the carrier mobility and anisotropy ratio (R_{ani}=max(μ_x, μ_y)/min(μ_x, μ_y)), while the method based on equation (2) usually overcorrects the carrier mobility in equation (1) and lowers the carrier mobility (relative to the experimental ones) and anisotropy noticeably[4], which can also be seen in Table S2. For example, the mobility of electrons in ML-Mo_2S_3 along x direction decrease from ~27000 $cm^2V^{-1}s^{-1}$ (SOC, or ~123000 $cm^2V^{-1}s^{-1}$ without SOC) to 907 $cm^2V^{-1}s^{-1}$ (SOC, or ~3509 cm^2V^-

^{1}s^{-1} without SOC). Moreover, it fairly reduces the anisotropy in the hole mobility between the x and y directions (from 34.2 to 1.7 for hole mobility along different directions in ML-Mo_2S_3). Thus, the corrected results in Table S2 can be used as a good reference.

Table S2. Calculated carrier mobility with different methods

Materials	Carrier type	Eq1			Eq2		
		μ_x (cm^{2}V^{-1}s^{-1})	μ_y (cm^{2}V^{-1}s^{-1})	R_{ain}	μ_x (cm^{2}V^{-1}s^{-1})	μ_y (cm^{2}V^{-1}s^{-1})	R_{ain}
Mo_2S_3	electron	123240	46	2679.13	3509	99	35.44
	hole	358	11104	31.02	731	344	2.13
Mo_2S_3 (SOC)	electron	27662	145	190.77	907	303	2.99
	hole	250	8551	34.2	506	301	1.68
Mo_2Se_3	electron	142398	204	698.03	3378	425	7.95
	hole	335	1956	5.84	683	109	6.27
W_2S_3	electron	96394	108	892.54	5094	223	22.84
	hole	761	21806	28.65	1547	844	1.83
W_2Se_3	electron	12219	22	571.47	11717	24	487.65
	hole	1448	2718	1.88	2719	342	7.96
MoS_2[4]	electron	115	111	1.04	110	114	1.04
	hole	289	314	1.09	290	313	1.08

μ_x and μ_y were calculated by setting the temperature to 300 K. "Eq1" and "Eq2" represent that the results were calculated by equation (1) and equation (2), respectively.

\

Table S3. Calculated carrier mobility compared with previous work.

Structure	**Carrier type**	**m_x^*/m_0 G-X**	**m_y^*/m_0 G-Y**	**E_{1x}**	**E_{1y}**	**C_x**	**C_y**	**μ_x**	**μ_y**
				(eV)		**(Jm^{-2})**		**($cm^2V^{-1}s^{-1}$)**	
SiS (Our results)	electron	0.16	0.51	4.91	1.5	63.13	115.04	1223	7493
	hole	0.24	6.34	3.75	1.4	63.13	115.04	324	160
SiS[2] **(Previous work)**	electron	0.16	0.50	4.77	1.33	67.60	111.50	1400	9490
	hole	0.24	5.92	3.71	1.52	67.60	111.50	366	146
Mo_2S_3 (soc)	electron	0.92	1.33	0.31	3.52	126.71	123.63	27662	145
	hole	0.35	1.2	6.91	0.63	126.71	123.63	250	8551
Mo_2S_3	electron	0.229	3.873	0.17	3.83	122.71	116.15	420342	46
	hole	0.271	1.176	6.79	0.58	122.71	116.15	371	11104

m_x^* and m_y^* are carrier effective masses for directions x and y, respectively; E_{1x} (E_{1y}) and C_x (C_y) are the deformation potential and 2D elastic modulus for the x (y) direction. μ_x and μ_y were calculated using equation (1) with the temperature T set to 300 K.

10. Transition from MoS_2 to Mo_2S_3

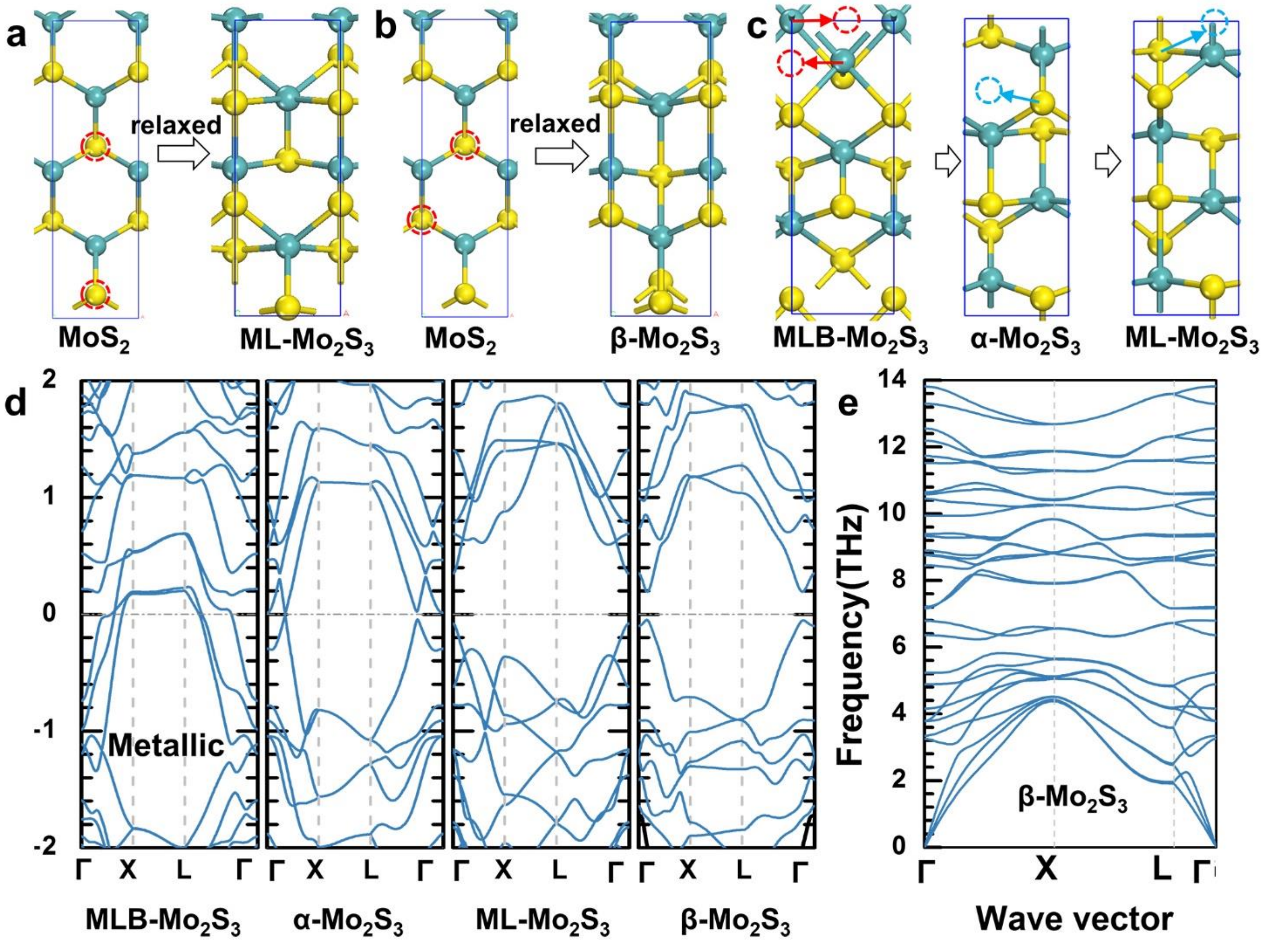

Fig. S18. Transition from monolayer MoS_2 and MLB-Mo_2S_3 (exfoliated from bulk Mo_2S_3) to monolayer Mo_2S_3 (labeled as ML-Mo_2S_3, obtained in our experiments). (a, b) DFT optimization of ML-Mo_2S_3 and β-Mo_2S_3 (another theoretically predicted structure) from MoS_2 by removing two S atoms per cell at different positions, as indicated by red dot circles. (c) Transformation from MLB-Mo_2S_3 to α-Mo_2S_3 (another theoretically predicted structure) and finally to ML-Mo_2S_3 (obtained in our experiments). The red and blue arrows/ circles indicate the moving of S atoms. (d) PBE calculated band structures of MLB-Mo_2S_3 (metallic), α-Mo_2S_3, ML-Mo_2S_3, and β-Mo_2S_3, respectively. (e) Phonon dispersion of the β-Mo_2S_3. There are no negative phonon frequencies in β-Mo_2S_3, which indicated that its structure is stable.

Table S4. Structural information and band gaps of different types of single layer Mo_2S_3

System	E_f	a	b	Symmetry	ΔE	E_g (PBE)	E_g (HSE)	W
	(eV)	(Å)			(eV)	(eV)		(eV)
MoS_2	-87.191	3.182	11.025	P-6m2	/	1.67	1.96	5.88
MLB-Mo_2S_3	-74.785	3.219	9.226	P21/m	0.000	0.00	/	4.49
α-Mo_2S_3	-75.372	3.258	9.319	P21/m	-0.587	0.00	/	5.10
ML-Mo_2S_3	-75.650	3.254	9.099	Pmc21	-0.865	0.42	0.90	5.44
β-Mo_2S_3	-75.435	3.195	9.424	Pm	-0.650	0.20	0.24	5.18
Exp-Mo_2S_3	/	3.171	9.027	Pmc21	/	/	/	/

ML-Mo_2S_3 is the theoretically predicted structure that accords well with our experimental results. ML-Mo_2S_3 exhibits the lowest formation energy (-75.650 eV/cell) than that of any other single layer form of Mo_2S_3. Exp-Mo_2S_3 is the structure obtained experimentally.

References

1 T. Joseph, M. Ghorbani-Asl, A. G. Kvashnin, K. V. Larionov, Z. I. Popov, P. B. Sorokin and A. V. Krasheninnikov, *J. Phys. Chem. Lett.*, 2019, **10**, 6492–6498.

2 J.-H. Yang, Y. Zhang, W.-J. Yin, X. G. Gong, B. I. Yakobson and S.-H. Wei, *Nano Letters*, 2016, **16**, 1110–1117.

3 H. Lang, S. Zhang and Z. Liu, *Phys. Rev. B*, 2016, **94**, 235306.

4 A. Rawat, N. Jena, D. Dimple and A. De Sarkar, *J. Mater. Chem. A*, 2018, **6**, 8693–8704.